New Journal of Physics
The open access journal at the forefront of physics

Deutsche Physikalische Gesellschaft DPG IOP Institute of Physics

PAPER • OPEN ACCESS

Transient dynamics of the quantum light retrieved from Rydberg polaritons

To cite this article: Auxiliadora Padrón-Brito *et al* 2021 *New J. Phys.* **23** 063009

New Journal of Physics
The open access journal at the forefront of physics

Deutsche Physikalische Gesellschaft DPG
IOP Institute of Physics

Published in partnership with: Deutsche Physikalische Gesellschaft and the Institute of Physics

OPEN ACCESS

RECEIVED
10 December 2020

REVISED
15 March 2021

ACCEPTED FOR PUBLICATION
27 April 2021

PUBLISHED
3 June 2021

PAPER

Transient dynamics of the quantum light retrieved from Rydberg polaritons

Auxiliadora Padrón-Brito[1,*], Roberto Tricarico[1], Pau Farrera[1,2], Emanuele Distante[1,2], Klara Theophilo[1], Darrick Chang[1,3] and Hugues de Riedmatten[1,3]

[1] ICFO-Institut de Ciencies Fotoniques, The Barcelona Institute of Science and Technology, 08860 Castelldefels, Barcelona, Spain
[2] Max-Planck-Institut für Quantenoptik, Garching, Germany
[3] ICREA-Institució Catalana de Recerca i Estudis Avaçats, 08015 Barcelona, Spain
[*] Author to whom any correspondence should be addressed.

E-mail: auxiliadora.padron@icfo.eu

Keywords: Rydberg atoms, single photons, electromagnetically induced transparency

Abstract

We study the photon statistics of weak coherent pulses propagating through a cold atomic ensemble in the regime of Rydberg electromagnetically induced transparency. We show experimentally that the value of the second-order autocorrelation function of the transmitted light strongly depends on the position within the pulse and heavily varies during the transients of the pulse. In particular, we show that the falling edge of the transmitted pulse displays much lower values than the rest of the pulse. We derive a theoretical model that quantitatively predicts our results and explains the physical behavior involved. Finally, we use this effect to generate single photons localized within a pulse. We show that by selecting only the last part of the transmitted pulse, the single photons show an antibunching parameter as low as 0.12 and a generation efficiency per trial larger than that possible with probabilistic generation schemes based on atomic ensembles.

1. Introduction

Highly excited Rydberg atoms enable long-range controllable atom–atom interactions [1]. This property has been used to demonstrate entanglement [2, 3] and quantum gates between individual atoms [4, 5] and more recently quantum simulation in atomic arrays [6, 7]. Besides using individual atoms, another approach currently investigated is to use collective Rydberg excitations in atomic ensembles, which on top of providing a medium with long-range controllable interactions also allows for an efficient quantum light–matter interface. Such an interface has led to remarkable demonstrations of optical nonlinearities at the single-photon level [8–10] that can be used for quantum nonlinear optics [11, 12] and quantum information applications, including single-photon level transistors and switches [13–15], 'contactless' photon–photon interactions [16] and gates [17]. Rydberg excitations can also be used to generate single photons in a quasi-deterministic fashion [18–21], contrary to ground state ensembles that usually rely on probabilistic or heralded schemes [22].

The use of electromagnetically induced transparency (EIT) with excited Rydberg levels [23] provides an efficient way of mapping light onto Rydberg excitations, leading to the creation of strong optical nonlinearities in the transmitted light thanks to the phenomenon of Rydberg blockade. Under EIT conditions, probe photons (characterized by the field E_p) resonant with a ground-to-excited state transition $|g\rangle \rightarrow |e\rangle$ can coherently propagate within a narrow transparency window with the use of an additional resonant control field (Ω_c) that couples $|e\rangle$ to a metastable state $|r\rangle$ (see figure 1(c)). In this process, the probe photons are mapped onto dark-state polaritons, propagating with a group velocity v_{gr} much smaller than the velocity of light in vacuum c. However, if $|r\rangle$ is a Rydberg level, the dipole–dipole interaction between Rydberg atoms prevents the excitation of two atoms to the Rydberg state if they are closer than a distance known as the blockade radius (r_b) [1], which destroys the EIT transparency condition for two

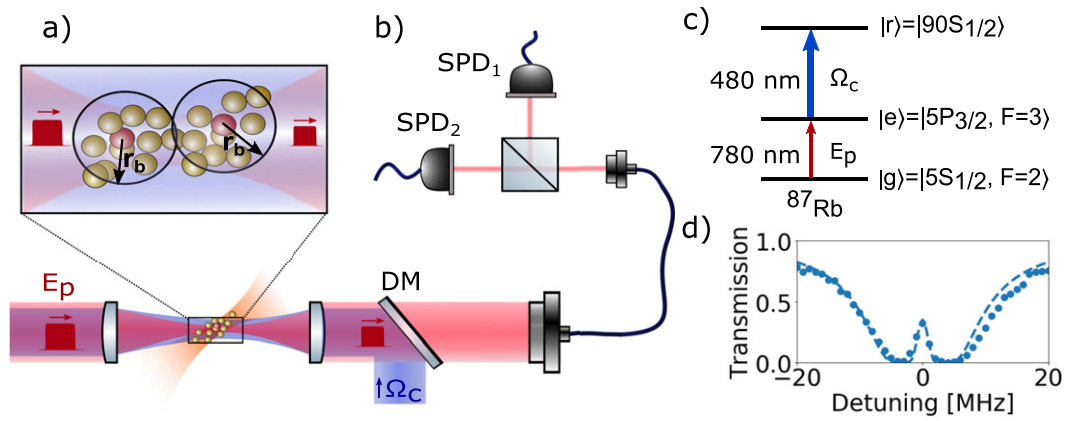

Figure 1. (a) Schematic representation of the experimental setup. A probe pulse (in red) in a focused Gaussian mode (shaded red) is incident on the atomic ensemble at a 19° angle relative to the dipole trap. The control beam (in blue) is sent in a counter-propagating direction relative to the probe, with both the probe and pump focused in the center of the dipole trap by two aspheric lenses. (b) The transmitted probe photons are sent through a Hanbury Brown and Twiss setup consisting of a beam-splitter and two single-photon detectors SPD_1 and SPD_2 to measure the second-order autocorrelation function. The various symbols in the figure refer to E_p: probe field amplitude, Ω_c: control field Rabi frequency, DM: dichroic mirror. (c) Atomic level scheme and transitions used in the experiment. (d) EIT transparency window measurement (points) and numerical simulation (dashed line) presented in section 4.4.

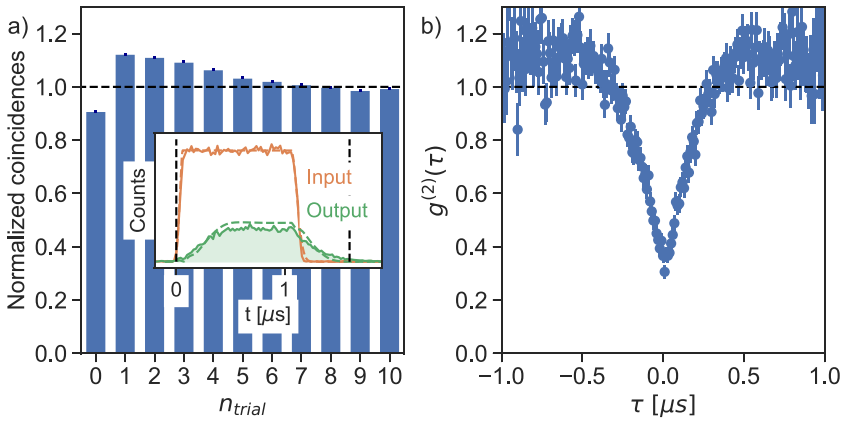

Figure 2. Photon statistics for a square pulse. (a) Normalized coincidences between the trial 0 and trial n_{trial}. The first value, corresponding to $n_{\text{trial}} = 0$, shows the normalized coincidences in the same trial, which gives a value of $g^{(2)}_{\Delta t}(0,0) = 0.908 \pm 0.004$. Inset in (a) shows the temporal distribution of the input (in orange) and the output pulse (in green). The solid lines indicate the experimental values and the dashed lines the results of the numerical simulations presented in section 4.4. The black lines delimit the temporal window with $\Delta t = 1.6\ \mu$s, longer than the output pulse duration. (b) Normalized coincidences with a bin size of $2\Delta t = 10$ ns, as a function of the delay time τ. The value at zero-delay time is $g^{(2)}(0) = 0.31 \pm 0.03$. Error bars in the plots correspond to one standard deviation.

propagating probe photons within the distance r_b. As a consequence, strong scattering and absorption associated with a resonant two-level medium occurs, whereby the probability of detecting two photons at the same time in the transmitted light mode is ideally reduced to zero. More concretely, the probability for two photons within a distance r_b to be transmitted decreases roughly as $\exp(-D_b)$, where D_b is the optical depth per blockade radius.

The transmission of weak, continuous-wave (CW) coherent input states of light through an ensemble of atoms under Rydberg EIT has been investigated theoretically [8, 24–27], and experimentally with the demonstration of single-photon-level nonlinearities and strong antibunching of the output light [8, 10]. However, the use of CW light makes it challenging to efficiently generate single photons localized in time, as required for some applications in quantum information science [28–30]. It has been shown that localized single photons can be retrieved from collective Rydberg excitations, which can be created by using an off-resonant two-photon excitation scheme [18, 20, 21, 31] or by storage of weak coherent light pulses under EIT conditions [19, 32]. However, this represents an additional experimental complexity and source of inefficiency. The use of transmitted pulses (without storage) in Rydberg EIT could therefore potentially lead to the generation of localized single photons with higher efficiencies, but the quantum statistics of weak

pulses traveling under Rydberg EIT conditions has not been well studied yet. Moreover, as shown in [18], reaching low values of $g^{(2)}(0)$ requires very high Rydberg levels and high values of D_b, which are experimentally hard to achieve, and low values of $g^{(2)}(\tau)$ are only observed for a small value of τ ($\sim$100 ns). Thus, reaching low values of $g^{(2)}$ for the entire pulse is challenging.

In this paper, we study experimentally and theoretically the propagation of weak coherent input pulses through a Rydberg EIT window. We measure the second-order autocorrelation function $g^{(2)}_{\Delta t}$ for short time windows Δt inside the pulse for various input pulse shapes. We show that the values of $g^{(2)}_{\Delta t}$ strongly vary during the transient phases, leading to very low values for the trailing edge, while the value for the full output pulse is much higher. Similar behavior of $g^{(2)}$ during the EIT transients has also been observed recently in reference [33]. Here, we perform a systematic experimental and theoretical investigation to better understand the underlying physics. We develop a theoretical framework that can quantitatively predict our experimental results and explain the physical behavior involved. In addition, we investigate the use of the transient regime for the production of higher quality narrowband single photons by measuring $g^{(2)}_{\Delta t}$ as a function of the photon generation efficiency and comparing the results with the single photons obtained via storage in the Rydberg states.

2. Experiment

Figure 1 shows a scheme of the experimental setup. A cloud of cold ^{87}Rb atoms is loaded in a dipole trap, with an atomic peak density of $\sim 4 \times 10^{11}$ cm^{-3} and a transverse size of 34 μm. The experimental sequence is the following: we start by loading a magneto-optical trap (MOT) for 2 s, followed by a compression of the MOT and a molasses period; the dipole trap is switched on 500 ms after the beginning of the MOT and it is switched off during the excitation of the atoms to the Rydberg level, to avoid losing atoms and remove AC stark shifts. This is done by modulating the dipole trap with a period of 16 μs, which leaves a time of less than 8 μs to perform one experimental trial. Each trial consists of a Rydberg EIT experiment. That is, every time the dipole trap is switched off, we send a probe pulse together with the control beam and measure the output photons. This is repeated 13 000 times during the dipole trap lifetime, which gives a total experimental rate of 5.73 kHz.

The atoms are initially prepared in the ground state $|g\rangle = |5S_{1/2}, F = 2\rangle$ and resonantly coupled with the state $|e\rangle = |5P_{3/2}, F' = 3\rangle$ by a weak probe field of 780 nm. The excited state is also resonantly coupled with the Rydberg state $|r\rangle = |90S_{1/2}\rangle$ using a counter-propagating control beam at 479.4 nm (see figure 1(c)). The probe beam is sent with an angle of 19° with respect to the dipole trap beam (see figure 1(a)) and propagates through the medium with an optical depth of $D \approx 10.6$. It is focused in the center of the atomic medium with a beam waist of $w_p \approx 6.5$ μm. Figure 1(d) shows the transmission spectrum of Rydberg EIT in our cloud, for an input photon rate $R_{in} \approx 0.3$ MHz. The other relevant parameters of the system are the spontaneous emission rate of the excited state $|e\rangle$, given by $\Gamma \approx 2\pi\times$ 6 MHz [34], a control field Rabi frequency of $2\Omega_c \approx 2\pi\times$ 6.4 MHz, and a dephasing rate of the Rydberg level of $\gamma_r \approx 2\pi\times$ 0.8 MHz. The resulting EIT bandwidth, giving the full width at half maximum of the resonant transmission peak, is $\delta_{EIT} \approx 2\pi \times 2.3$ MHz, while the EIT group velocity is $v_{gr} \approx 200$ μm μs^{-1} and the EIT delay time for a pulse to propagate through the medium is $\tau_{EIT} \approx 0.5$ μs. Thus the average number of input photons in the medium during this propagation time is no more than $R_{in}\tau_{EIT} \approx 0.15$. For such low photon numbers, nonlinear effects associated with Rydberg interactions have negligible effect on the transmission spectrum, and the deviation from unit transmission on EIT resonance in figure 1(d) is attributable to the dephasing rate of the Rydberg state γ_r. The blockade radius for our experimental parameters is $r_b \approx 13$ μm, which is larger than the probe beam waist and thus restricts photon interaction dynamics to the same transverse mode. The optical depth per blockade radius is $D_b \approx 0.9$.

We characterize the quantum correlations of the output light via the second-order autocorrelation function, defined as:

$$g^{(2)}(t,\tau) = \frac{\langle E^\dagger(t)E^\dagger(t+\tau)E(t+\tau)E(t)\rangle}{\langle E^\dagger(t)E(t)\rangle \langle E^\dagger(t+\tau)E(t+\tau)\rangle}, \quad (1)$$

where $E(t)$ is the electric field operator for the transmitted light at time t. We measure the second-order autocorrelation function by sending the output pulses through a Hanbury Brown and Twiss setup, which consists of a beam splitter and two single-photon avalanche detectors (SPDs), as shown in figure 1(b). The arrival times of the photons for each detector, together with trigger times for each trial, are saved in a time-stamp file.

Experimentally, we estimate the idealized definition of the autocorrelation function in equation (1) by first selecting a detection time window Δt. Then, $g^{(2)}_{\Delta t}(t,\tau)$ is obtained from the equation

$$g^{(2)}_{\Delta t}(t,\tau) = \frac{P_{12,\Delta t}(t,t+\tau)}{P_{1,\Delta t}(t)P_{2,\Delta t}(t+\tau)}, \quad (2)$$

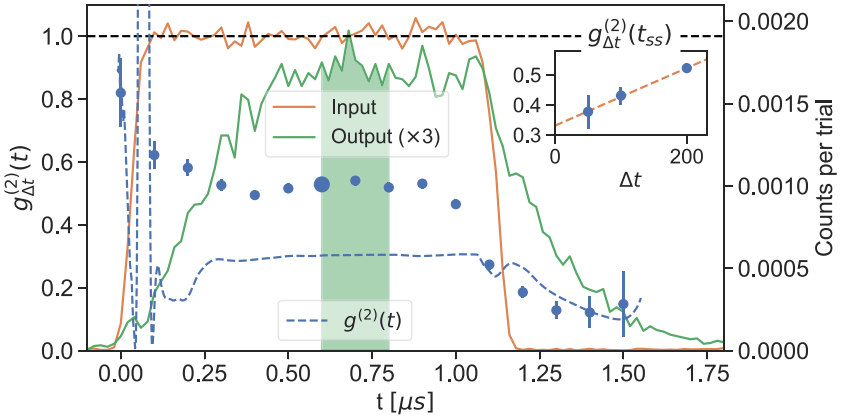

Figure 3. Transient photon statistics for a square pulse. The counts per trial (right y-axis) of the input (orange) and output (green) pulses are shown with respect to the arrival time at the photodetector. An example of the $\Delta t = 200$ ns window that we take to calculate $g^{(2)}_{\Delta t}(t)$ is shaded in green. The measured second-order autocorrelation function (blue points, left y-axis) is shown for different starting times t of the 200 ns window along the output pulse. The highlighted point (larger blue data point) corresponds to the shaded region. The dashed blue line shows the second-order correlation function obtained from the numerical simulation of $g^{(2)}(t)$ presented in section 4.4, which corresponds to the case of $\Delta t \to 0$. For comparison, in the top-right inset we show that the average ss experimental value $g^{(2)}_{\Delta t}(t_{ss})$ tends to the theoretical $g^{(2)}_{ss}(t) \approx 0.3$ for smaller Δt (the dashed orange line is a linear fit to guide the eye). Note that there are a number of fine temporal features in the theoretically calculated $g^{(2)}(t)$, which are not observed experimentally. This could be due to the relatively large values of Δt used in the experiment, which would smooth out such features. The error bars correspond to one standard deviation.

where t is the starting time of the detection window in the detector SPD_1 and $t + \tau$ is the starting time in the detector SPD_2, both measured with respect to the trigger time. $P_{12,\Delta t}(t, t+\tau)$ is the coincidence probability between the two detectors and $P_{1,\Delta t}(t)$ and $P_{2,\Delta t}(t+\tau)$ are the detection probabilities in detector SPD_1 and SPD_2, respectively. The normalization factor $P_{1,\Delta t}(t)P_{2,\Delta t}(t+\tau)$ is obtained by averaging the number of coincidences between photons arriving to the first detector in one trial and the photons arriving to the second detector from the 5th to the 20th following trials, where there is no correlation (see figure 2(a)). The correlation between the first five trials can be explained by the creation of long-lived pollutants [35, 36]. The transmission efficiency from the ensemble to the first detector is 0.23 ± 0.02, taking into account all the optical elements, and the SPD_1 detection efficiency is 0.43 ± 0.04.

3. Time-resolved photon correlation

First, we study the photon statistics for the case of a square pulse with a temporal length of 1 μs and a mean number of photons of ≈ 1.5, propagating through the Rydberg medium under EIT conditions. This corresponds to a mean number of photons in the medium at a time of 0.8. In the inset of figure 2(a), we plot the temporal shape of the input and output pulses, showing an EIT transmission efficiency of $\eta = N_{out}/N_{in} = 0.285 \pm 0.016$, where $N_{out(in)}$ is the total number of counts in the output(input) pulse. Figure 2(a) shows an example of the autocorrelation measurement for $\Delta t = 1.6$ μs, sufficiently large to include the whole output pulse (see the detection window delimited by the black dashed lines of the inset). The normalized coincidences for the trial number $n_{trial} = 0$ lead to $g^{(2)}_{\Delta t}(0,0) = 0.908 \pm 0.004$, which shows that while the full output pulse displays quantum statistics, it is still far from being a single photon.

We then select a small detection window of $\Delta t = 5$ ns and integrate the numerator and denominator of $g^{(2)}_{\Delta t}(t,\tau)$ (see equation (2)) over all the possible values of t within the pulse duration. We refer to this quantity as $g^{(2)}(\tau)$. The results are shown in figure 2(b). For $\tau = 0$, we obtain $g^{(2)}(0) = 0.31 \pm 0.03$, demonstrating the single-photon nature of the output light, as shown previously in [8, 13–15, 19]. However, we see that $g^{(2)}(\tau)$ quickly increases to 1 for $\tau \geqslant 350$ ns, much shorter than the pulse duration. We note that a time of $\tau = 350$ ns corresponds to a spatial distance of 70 μm $\gg r_b$, given the EIT group velocity v_{gr}. The fact that the distance exceeds the blockade radius can be explained by a diffusion effect that arises due to the narrow spectrum of the EIT transparency window [8].

To get a better understanding of the dynamics of Rydberg polaritons, we perform a more detailed study of the second-order autocorrelation function within a pulse. To this end, we select a detection window Δt much shorter than the pulse duration and we measure the zero-delay autocorrelation function $g^{(2)}_{\Delta t}(t,0)$ as a function of the starting time of the detection window t. For simplicity, $g^{(2)}_{\Delta t}(t,0) \equiv g^{(2)}_{\Delta t}(t)$ henceforth. An example is shown in figure 3 where we show the $g^{(2)}_{\Delta t}(t)$ (blue points), obtained by taking a window of $\Delta t = 200$ ns (green shadowed region), for different positions of this window throughout the output pulse.

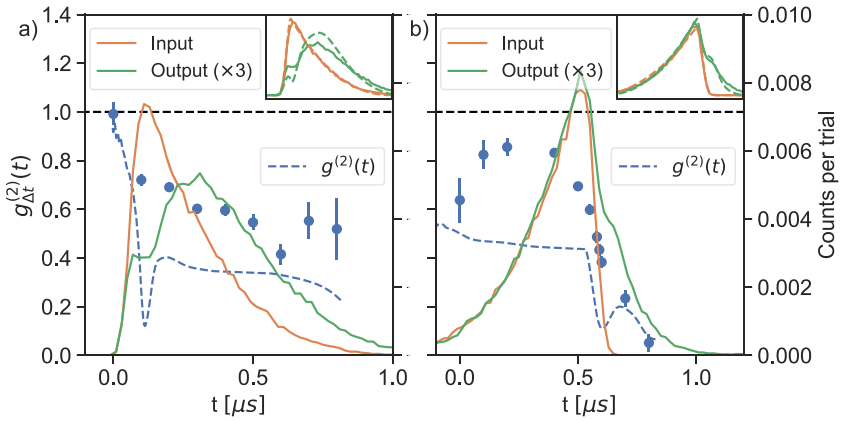

Figure 4. Transients for triangular pulses. Second-order autocorrelation function (in blue) for a detection window Δt of 200 ns along the output pulse, along with the temporal distribution of the input (in orange) and output (in green) counts for triangular shape pulses with negative (a) and positive (b) slope. The error bars correspond to one standard deviation. The dashed blue line shows the second-order correlation function obtained from the numerical simulation of $g^{(2)}(t)$, which corresponds to the case of $\Delta t \to 0$. The dashed lines in the top-right insets indicate the simulated input and output intensities. The details of the numerical simulations are presented in section 4.5.

One of our main results is that we find that the second-order autocorrelation function is not constant throughout the pulse duration, but decreases towards the end of the pulse. In fact, we observe three different regimes. For early times ($t < 0.4$ μs), a first transient associated with the rapid turn-on of the pulse is observed, exhibited by a decrease in $g^{(2)}_{\Delta t}(t)$ and an increase in the output intensity over time. We measure $g^{(2)}_{\Delta t}(t) = 0.8 \pm 0.1$ for $t = 0$ and $g^{(2)}_{\Delta t}(t) = 0.53 \pm 0.02$ for $t = 0.3$ μs. In the steady-state (ss) region (0.4 μs $< t < 1$ μs), both $g^{(2)}_{\Delta t}(t)$ and the output intensity are constant over time. Note that in this region, the value of $g^{(2)}_{\Delta t}(t)$ decreases as we decrease the time window Δt, as shown in the top-right inset of figure 3. This is because lowering Δt effectively narrows the range of possible delay times τ between two photons (see figure 2(b)), while Rydberg blockade makes the detection of directly overlapping photons in time improbable. Finally, when the input pulse is switched off ($t > 1$ μs), a second transient is observed. Although a decrease in the output intensity is expected, $g^{(2)}_{\Delta t}(t)$ follows the same behavior in the same time range, decreasing until reaching a value as low as $g^{(2)}_{\Delta t}(t) = 0.12 \pm 0.05$ for $t = 1.4$ μs. These distinct behaviors of $g^{(2)}_{\Delta t}(t)$ during the turn-on, steady state, and turn-off periods can be understood theoretically, as we will describe in the section 4.

To show the dependence of these transients with the shape of the input pulse, we also study the propagation of triangular pulses (see figure 4), following the same method described above. For this set of measurements, $D \approx 5.5$, $2\Omega_c \approx 2\pi \times 6.0$ MHz, $\gamma_r \approx 2\pi \times 1.0$ MHz, and the mean number of photons per pulse is < 0.5. In the case of a triangular shape with a negative slope (see figure 4(a)), the probe field is switched on abruptly but slowly switched off. Here, we observe that $g^{(2)}_{\Delta t}(t)$ starts with a value close to 1, but then it decreases rapidly towards smaller values, remaining nearly constant at the end of the pulse with $g^{(2)}_{\Delta t}(t) = 0.52 \pm 0.13$ for the last point ($t = 0.8$ μs). For a triangular shape with a positive slope (see figure 4(b)), i.e. slowly switched on and abruptly turned off, we only observe a clear transient at the end of the pulse, since $g^{(2)}_{\Delta t}(t)$ starts to decrease when the input pulse intensity goes to zero ($t > 1$ μs). A value of $g^{(2)}_{\Delta t}(t) = 0.05 \pm 0.04$ is obtained for the last point ($t = 0.8$ μs), which is much lower than the observed value for the triangular shape with negative slope.

These results show that the appearance of the transients depends on how the input pulse varies over time. Specifically, very low values of $g^{(2)}_{\Delta t}(t)$ are observed at the end of the pulse only if the decrease in intensity of the input pulse is fast enough.

4. Theoretical model

Here, we numerically analyze the transient behavior observed experimentally and also provide an intuitive model that elucidates the underlying physics in the simplest case of a fully blockaded medium. Afterward, we use this model to understand the experimental results. We first briefly discuss our numerical 'spin model' technique. The features of the output field are expected to only depend on the control field Ω_c, on the optical depth D of the entire medium and on the optical depth D_b per blockade radius, but not on the total number of atoms or on the per-atom coupling efficiency of the probe mode separately. Taking advantage of this observation, it is then possible to investigate an artificial, quasi-one-dimensional system of

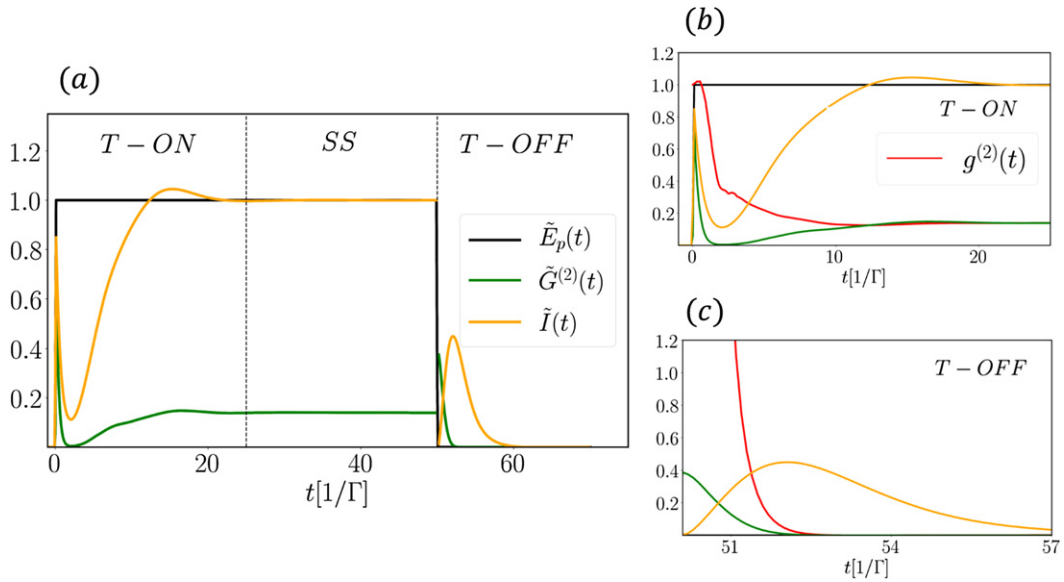

Figure 5. Analysis of the dynamics of a weak square input pulse for a control Rabi frequency of $\Omega_c = \Gamma/2$, $D \approx 3.6$ and a fully blockaded system. (a) The normalized output intensity $\tilde{I}(t)$ as a function of time (yellow) and the correlation function $\tilde{G}^{(2)}(t)$ (green). The intensity of the input pulse $\tilde{E}_p$ (normalized to unity) is also shown in black for reference. Three distinct regions in the dynamics can be observed, turn-on (T-ON), steady state (SS) and turn-off (T-OFF). (b) Normalized second-order correlation function $g^{(2)}(t)$ (red), output intensity $\tilde{I}(t)$ (yellow) and $\tilde{G}^{(2)}(t)$ (green) in the turn-on stage, with the input again shown for reference (black). (c) $g^{(2)}(t)$ (red), $\tilde{I}(t)$ (yellow) and $\tilde{G}^{(2)}(t)$ (green) in the turn-off stage.

a much smaller, tractable number of atoms with increased coupling efficiency to the probe, while maintaining the same D, D_b of the experiment. In all subsequent numerical simulations, we fix the optical depth per atom on the $|g\rangle$–$|e\rangle$ transition (absent EIT) to be $D_{atom} \approx 0.36$ and vary the number of atoms to tune D. Furthermore, the dynamics of the atomic internal degrees of freedom ('spins') are encoded in an interacting spin model, whose solution can be used to re-construct all field properties via an input–output formalism. Details of this formalism can be found in references [37, 38] and its previous application toward modeling Rydberg EIT experiments is described in reference [35]. Our numerical calculation truncates the Hilbert space to two total atomic excitations (in the states $|e\rangle$ and/or $|r\rangle$) and ignores quantum jumps, which is valid in the regime of weak probe light [37]. Moreover, we will restrict ourselves to the case where the probe field and the control field are resonant with the $|g\rangle$–$|e\rangle$ and $|e\rangle$–$|r\rangle$ transitions, respectively.

Analytically, we consider the simplest model where similar transient behavior can be observed, consisting of the limit where the probe input field $E_p(t)$ approaches a square pulse with amplitude E_{p_0} when turned on and where the system is fully blockaded, so that two atoms cannot simultaneously be in the Rydberg state $|r\rangle$. We consider a square pulse long enough that all observables equilibrate to a ss value at some point during the period where the pulse is turned on, and we assume that the dephasing of the Rydberg state is negligible. We note that the calculated transmittance and second-order correlation functions are independent of the specific value of E_{p_0} used in the simulations, provided that we restrict to a 'weak driving regime' where the two-excitation population is negligible compared to the single-excitation one. In figure 5 we show a representative plot versus time of the normalized output intensity $\tilde{I}(t) = \langle\psi|E^\dagger(t)E(t)|\psi\rangle/E_{p_0}^2$, the normalized 'two-photon intensity' $\tilde{G}^{(2)} = \langle\psi|E^{\dagger 2}(t)E^2(t)|\psi\rangle/E_{p_0}^4$ and the normalized second-order correlation function at zero delay $g^{(2)}(t,0) = \tilde{G}^{(2)}(t)/\tilde{I}^2(t) \equiv g^{(2)}(t)$. We can clearly identify three separate regimes of behavior: the initial turn-on, the steady state and the final turn-off. Below, we analyze each regime separately in more detail.

4.1. Steady state

We begin with the ss properties, which have already been extensively studied in reference [8]. First, we note that in the weak driving regime, the output intensity is predominantly dictated by the single-excitation component of the atomic system (since the one- and two-photon populations of the incoming pulse scale like E_p^2 and E_p^4, respectively). As the single-photon component does not experience Rydberg nonlinearities and sees perfect transparency associated with EIT, it results that the normalized intensity $\tilde{I}(t) \approx 1$ in the steady state (yellow curve in figure 5(a)). On the other hand, the two-photon intensity $\tilde{G}^{(2)}$ is efficiently attenuated due to the destruction of the EIT transparency condition by the Rydberg blockade. For a fully blockaded medium, the ss value of the output second-order correlation function was proved to be

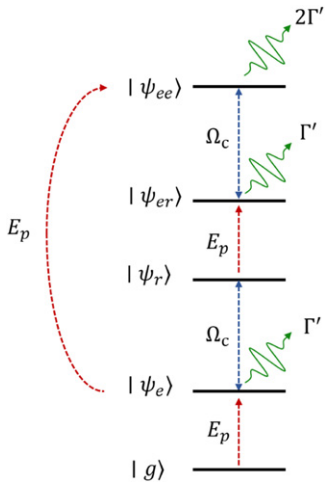

Figure 6. Schematic representation of the atomic level scheme for a fully blockaded medium in the weak driving regime. Within the single-excitation manifold, one atom can either be in the excited state $|e\rangle$ or in the Rydberg state $|r\rangle$, as represented by the subspaces $|\psi_{e,r}\rangle$, respectively. Similarly, in the two-excitation manifold, either one atom can occupy the state $|e\rangle$ while another one the state $|r\rangle$, or two atoms can simultaneously occupy the state $|e\rangle$. The pathways by which the subspaces can become excited by either the probe (E_p) or by the control field (Ω_c) are indicated by dashed arrows, while the free-space emission rates due to decay of the excited state $|e\rangle$ by green wavy arrows.

decreasing with D and increasing with Ω_c and to admit the following approximate expression in the limit of high optical depth: $g_{ss}^{(2)} \approx 4\frac{1+(\Omega_c/\Gamma)^2}{\pi D}\exp\left[\frac{-D}{1+(\Omega_c/\Gamma)^2}\right]$ [8].

4.2. Turn-on

Once we switch the probe field suddenly on at $t = 0$, the system evolves toward the ss configuration. In figure 5(b), we show a representative plot of $g^{(2)}(t)$ during this transient period. To further understand the behavior, it is convenient to utilize an input–output relation, which formally allows one to express the output field operator as a sum of the input field and the field re-emitted by the atoms. In a quasi-one-dimensional propagation problem, this takes the form [37, 38]:

$$E = E_p(t) - i\sqrt{\frac{\Gamma_{1D}}{2}}\sum_{h=1}^{N} e^{ik_p z_h}\sigma_{ge}^h. \tag{3}$$

Here, $\sigma_{ge}^h = |g_h\rangle\langle e_h|$ is the atomic lowering operator associated with atom h, $|g_h, e_h\rangle$ are its ground and excited states, respectively, z_h is the position of atom h, and $k_p \approx \omega_{eg}/c$ is the probe beam wavevector, where c is the speed of light in vacuum. We have normalized the field such that $E^\dagger E$ has units of photon number per unit time and Γ_{1D} is the emission rate of atoms into the Gaussian mode defined by the input probe beam. The spontaneous decay rate Γ of the excited state is decomposed into the sum of Γ_{1D} and Γ', where Γ' is the decay rate into noncollectable directions and represents the losses. The optical depth reads $D = 2N\log\left(\frac{\Gamma_{1D}+\Gamma'}{\Gamma'}\right)$, and in our spin model simulations we fix $\Gamma_{1D}/\Gamma' = 0.2$, so that the optical depth per atom results to be $D_{atom} \approx 0.36$. Since the atoms are initially in the ground state and the atomic properties must evolve continuously, one finds $\sigma_{ge}^h|\psi(t = 0^+)\rangle = 0$ at a time $t = 0^+$ immediately after the turn-on of the pulse. From equation (3), this implies that the output field is the same as the input field immediately after turn-on, and in particular, $g^{(2)}(0^+) = 1$ reflects the coherent-state statistics of the input field. This also causes the first peak in the transmitted intensity immediately after turn-on, shown in figure 5(b), which can alternatively be thought as arising from frequency components of the input field during the turn-on that are too far detuned to interact with the atoms.

We now characterize the time scale τ_0 over which $g^{(2)}(t)$ is expected to approach its ss value, $g^{(2)}(\tau_0) \sim g_{ss}^{(2)}$. To do so, it is helpful to draw a schematic of the possible atomic levels that can be excited in the weak-probe limit (up to two excitations), as indicated in figure 6. Here, we denote $|\psi_{e,r}\rangle$ as the manifold of states where only one atom is excited to states $|e\rangle$, $|r\rangle$, respectively. Similarly, $|\psi_{er,ee}\rangle$ denote the manifold of states where one atom is in $|e\rangle$ while another is in $|r\rangle$, or two atoms are in the state $|e\rangle$ (recall that we consider a fully blockaded medium, so two atoms cannot occupy state $|r\rangle$). We denote with dashed arrows the possible paths by which these states can be excited by the probe and control fields. We have also

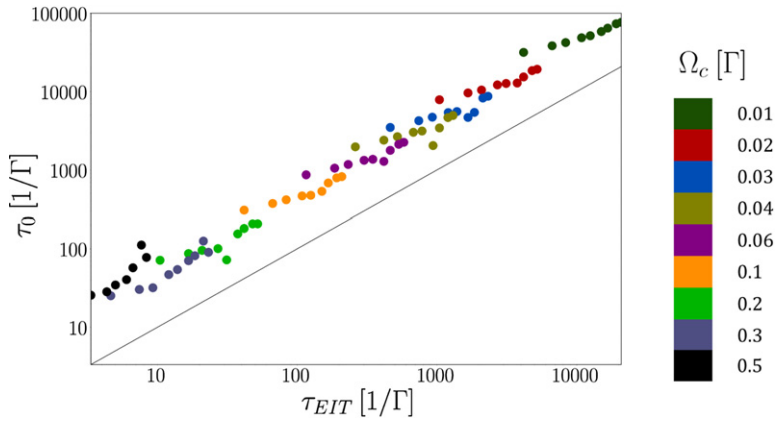

Figure 7. Relationship between the turn-on transient time τ_0 and the EIT propagation time $\tau_{\rm EIT}$ (black solid line). τ_0 is defined as the time after which $\left|g^{(2)}(t)-g^{(2)}_{\rm ss}\right|/g^{(2)}_{\rm ss}<0.005$. Different values of $\tau_{\rm EIT}=D\Gamma'/4\Omega_{\rm c}^2$ are sampled by varying the optical depth D in simulations from 1.8 to 9.1 and the control field $\Omega_{\rm c}$ from $\Gamma/100$ to $\Gamma/2$. The values of $\Omega_{\rm c}$ are indicated by the different colors, as represented in the colorbar to the right.

indicated by the wavy green arrows the rates of dissipation of these states due to spontaneous emission into 4π.

In the limit of a weak probe beam, the population of the two-excitation manifold is sufficiently small that its back-action onto the evolution of the single-excitation manifold can be neglected. Furthermore, since the coupling of the probe and control fields between the ground state and the single-excitation manifold behave as if they were undergoing EIT in the linear optics regime, their dynamics are straightforward to analyze. In particular, the square pulse should propagate through the system at the reduced EIT group velocity $v_{\rm gr}$ and its leading-edge should reach the end of the medium in a time $\tau_{\rm EIT}=L/v_{\rm gr}=D\Gamma'/4\Omega_{\rm c}^2$. The single-excitation manifold effectively acts as a source to populate the two-excitation one (see figure 6), and the two-excitation manifold should reach the steady state within a time $\sim\Gamma^{-1}$ of the single-excitation manifold doing so, due to the spontaneous emission rate of states within this manifold (see wavy green arrows in figure 6). As this time scale is negligible, we then expect that $\tau_0\approx\tau_{\rm EIT}$.

In figure 7, we confirm this scaling numerically. In particular, we vary both the control field amplitude $\Omega_{\rm c}$ and optical depth D over a large range of values. We further define τ_0 as the time in which the numerically obtained fractional difference between the transient value of the second-order correlation function and its ss value $|g^{(2)}(\tau_0)-g^{(2)}_{\rm ss}|/g^{(2)}_{\rm ss}$ drops below 0.005. We see that $\tau_0\approx\tau_{\rm EIT}$ over the entire range of parameters studied, and independent of the specific values of D and $\Omega_{\rm c}$ separately.

4.3. Turn-off

In figure 5(c) we show the output $\tilde{I}$, $\tilde{G}^{(2)}$ and $g^{(2)}$ when we switch the probe field suddenly off, starting from a ss initial condition. The dynamics exhibits two notable features. First, discontinuities can develop in the observables immediately after the shutoff. Second, one sees that the second-order correlation function $g^{(2)}(t)$ approaches zero at sufficiently long times, indicating a stronger antibunching than the one realizable in the steady state. We begin by analyzing the dynamics in the vicinity of the shutoff of the probe, which we define to occur at the time $\bar{t}$.

Using the input–output relation of equation (3), one sees that the output field operator E evolves discontinuously. In particular, the outgoing intensity at a time $\bar{t}^+$ immediately following the shutoff, $\langle E^\dagger(\bar{t}^+)E(\bar{t}^+)\rangle$, will only be due to purely atomic emission and jump from its value at $\bar{t}^-$ immediately before the shutoff. Furthermore, since this intensity is dominated by the single-excitation component for weak driving, and as the $|e\rangle$-state component of this manifold is unpopulated ($|\psi_e\rangle=0$) due to perfect EIT, the atoms are not able to emit light instantaneously and one finds $\tilde{I}(\bar{t}^+)\approx 0$. Conversely, the normalized two-photon intensity $\tilde{G}^{(2)}$ experiences a discontinuous increase. In ss conditions and high optical depth, its value $\tilde{G}^{(2)}_{\rm ss}\ll 1$ can be understood from equation (3) as nearly perfect destructive interference between the incoming field and the field re-emitted by the atoms, since two photons cannot be efficiently transmitted due to the Rydberg blockade. Therefore, if the input field is instantly extinguished, the two-photon outgoing intensity is due to a purely atomic emission which, for large D, is almost equal in amplitude (but opposite in phase) to the incoming field. As a consequence, one expects that $\tilde{G}^{(2)}(\bar{t}^+)\to 1$ and $g^{(2)}(\bar{t}^+)\to\infty$ in the square pulse limit. For a continuous switch off, a flash of bunched output light can still

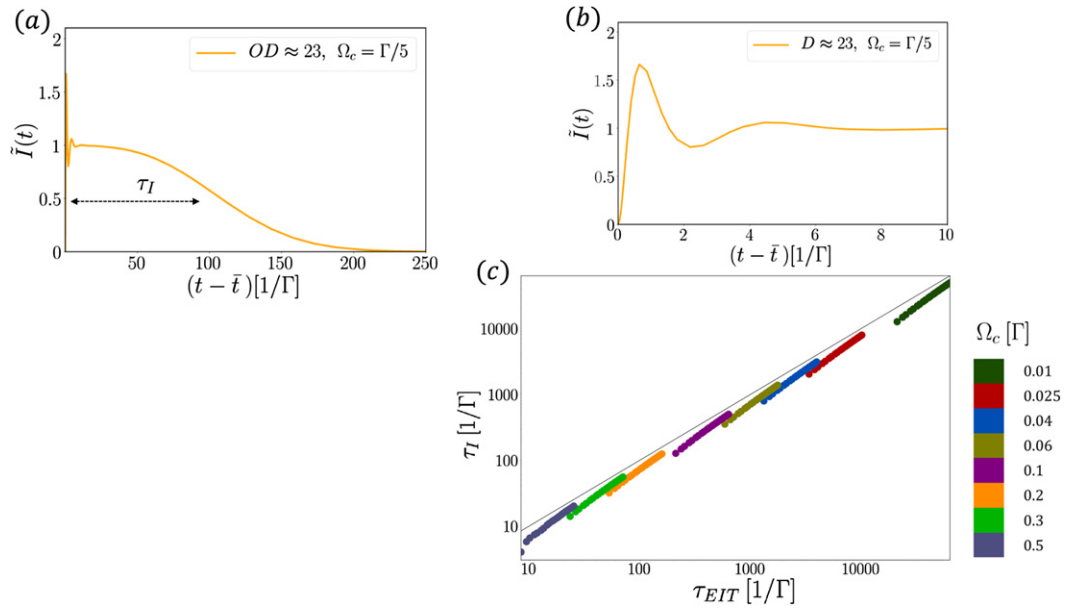

Figure 8. Analysis of the single-excitation dynamics in the turn-off regime. (a) Representative plot of the normalized output intensity $\tilde{I}(t)$ for $D \approx 23$ and $\Omega_c = \Gamma/5$. The single-excitation characteristic time τ_I is defined as the amount of time needed, following the turn-off (occurring at time $\bar{t}$), for the normalized intensity to drop to half of its ss value, $\tilde{I}(\bar{t}+\tau_I) = 0.5$. (b) Detail of the short times dynamics. (c) Relationship between τ_I and the EIT propagation time τ_{EIT} sampled by varying D form 9.1 to 27.3 and Ω_c from $\Gamma/100$ to $\Gamma/2$. The values of Ω_c are indicated by the different colors, as represented in the colorbar to the right.

emerge if the time scale of the shutoff is faster than the time needed by the atoms to react, which is roughly $\sim \Gamma^{-1}$ [33].

The analysis of the transient dynamics following the instant shutoff of the probe is made easier by noting that the single- and the two-excitation components of the atomic system become decoupled when $E_p = 0$ (see figure 6) and we can thus investigate the dynamics in each manifold separately. Immediately following the shutoff, any atomic excitation in the single-excitation manifold takes the form of a spin wave in the Rydberg state $|\psi_1(\bar{t}^+)\rangle = |\psi_1^{ss}\rangle \sim \sum_h e^{ik_p z_h}|r_h\rangle$ due to the perfect EIT condition. This makes the subsequent dynamics equivalent to the retrieval of a stored spin wave in an EIT-based quantum memory. We will restrict ourselves to the regime of reasonably high D and small Ω_c, such that the retrieved field takes a similar spatial form as the spin wave itself (in contrast when $\Omega_c \geqslant \Gamma$, the outgoing pulse can oscillate due to Rabi flopping dynamics between $|e\rangle$ and $|r\rangle$). In figure 8(a), we show a representative plot of the output intensity as a function of time following the shutoff, for $D \approx 23$ and $\Omega_c/\Gamma = 0.2$. Due to the finite bandwidth of the EIT transparency window, the shape of the retrieved output intensity is smoother than the flat rectangular shape of the ss spin wave itself. We define a characteristic time τ_I as the amount of time following the shutoff for the normalized outgoing intensity to reach half of its ss value, $\tilde{I}(\bar{t}+\tau_I) = 0.5$. We expect that $\tau_I \approx \tau_{EIT}$, i.e. τ_I should approximately coincide with the time needed to propagate across the medium at the reduced EIT group velocity. In figure 8(c), we plot the numerically extracted τ_I over a broad range of optical depths and control field amplitudes and see a good agreement with the expected result. Finally, we remark that at short times following the shutoff, the outgoing intensity can exceed the ss intensity of the original square wave input, $\tilde{I}(t) > 1$, as illustrated in figure 8(b). Physically, at short times, the control field can drive the original spin wave stored in the state $|r\rangle$ into a 'bright' spin wave $\sim \sum_h e^{ik_p z_h}|e_h\rangle$. It is known that such a spin wave experiences collectively enhanced or superradiant emission into the forward direction [39, 40], at a rate $\sim \Gamma D/4$, which physically arises from the constructive interference between the light emitted by different atoms in this direction due to their relative phases $\sim e^{ik_p z_h}$.

We now turn to the two-photon intensity. In figure 9(a) we show a representative plot of the output $\tilde{G}^{(2)}(t)$ at the turn-off. One sees that at short times it rapidly decays to zero with a hump-like profile, while at long times it exhibits slower oscillating features. We define a characteristic temporal length of the short time behavior, τ_{II}, as the amount of time for the normalized two-photon intensity to reach half of its value immediately after turn-off, $\tilde{G}^{(2)}(\bar{t}+\tau_{II}) = \tilde{G}^{(2)}(\bar{t})/2$. Numerically, we find that τ_{II} scales like $1/D$, as shown in figure 9(b). This can be understood as both the *er* and the *ee* components of the two-excitation ss wave function $|\psi_2^{ss}\rangle$ are phase-matched and emit in a collectively enhanced fashion immediately after turn-off. However, as $|\psi_2^{ss}\rangle$ is not an eigenstate of the system, it can undergo spatio–temporal evolution. At long

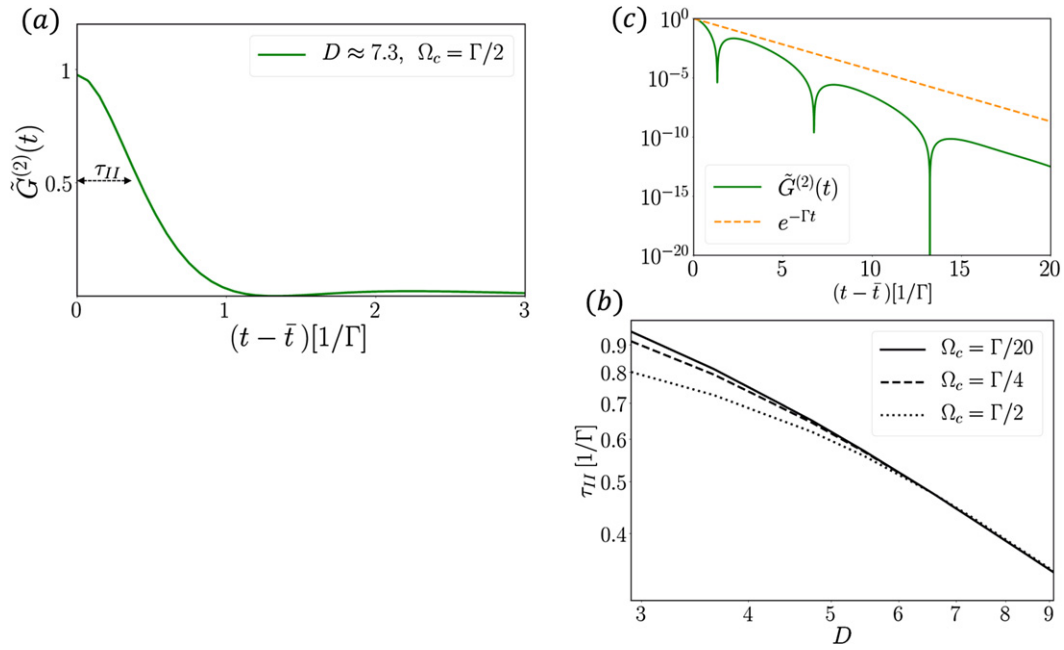

Figure 9. Analysis of the double-excitation dynamics in the turn-off regime. (a) Representative plot of the normalized output two-photon intensity $\tilde{G}^{(2)}(t)$ for $D \approx 7.3$ and $\Omega_c = \Gamma/2$. The double-excitation characteristic time τ_{II} is defined as the amount of time needed, following the turn-off (occurring at time $\bar{t}$), for the normalized two-photon intensity to drop to half value immediately after turn-off, $\tilde{G}^{(2)}(\bar{t}_{II}) = \tilde{G}^{(2)}(\bar{t})/2$. (b) The double-excitation characteristic time τ_{II} sampled by varying D from 2.9 to 9.1 for $\Omega_c = \Gamma/20, \Gamma/4$, and $\Gamma/2$. (c) Long time profile of $\tilde{G}^{(2)}(t)$, along with the single-atom spontaneous decay dynamics $e^{-\Gamma t}$ for reference (dashed yellow line).

times, the emitted two-photon intensity will thus no longer be collectively enhanced but will decay at a rate $\sim \Gamma$ comparable to the single-atom decay rate. This behavior can be seen in figure 9(c), by comparing the envelope of $\tilde{G}^{(2)}$ at long times with $e^{-\Gamma t}$.

We can now finally understand why $g^{(2)}(t) = \tilde{G}^{(2)}(t)/\tilde{I}(t)^2$ decreases below its ss value at long times after the turn-off. In particular, with increasing optical depth, the numerator $\tilde{G}^{(2)}(t)$ describing the two-excitation component rapidly decays on a time scale $\tau_{II} \propto 1/D$ due to collective enhancement (with a small residual component decaying at the single-atom rate $\sim \Gamma$), while the denominator persists for a longer time $\tau_I \propto D$ due to the slow retrieval dynamics of the single-excitation component.

4.4. Simulation of the experiment—rectangular pulse

To reproduce the experimental measurements of the square pulse dynamics, we add the motional dephasing γ_r of the Rydberg atoms to the numerical simulation, incorporating it into an effective decay rate of the states $|r\rangle$. By setting D, Ω_c, Γ, and γ_r to the values given in section 2, the numerical results obtained for the linear transmission are in good agreement with the experimental EIT transmission and with the output counts, shown in figures 1(d) and 2 (a), respectively. Moreover, we remove the fully blockaded hypothesis and model the finite blockade with an interaction potential of the form $V_r = V_0(r_b/r)^6$, where r_b is the blockade radius and $V_0 = 2\Omega_c^2\left[\Gamma_{1D}\left(2\Gamma' + \Gamma_{1D}\right)\right]^{-1/2}$ is the single-atom bandwidth. By setting D_b to the value in section 2, one finds $g_{ss}^{(2)} \approx 0.3$, which is in agreement with the $\tau = 0$ value of figure 2(b). In figure 3, the resultant pulse analysis is shown, and it is worth noticing how the measured $g_{\Delta t}^{(2)}(t)$ tends towards the numerically predicted $g^{(2)}(t)$ as one decreases the length of the detection window Δt (as shown in the top-right inset of figure 3).

In order not to affect the validity of the truncation of the Hilbert space to the double-excitation manifold, the maximum input field amplitude E_{p_0} in the simulations must be small enough to keep the two-excitation population negligible compared to the single-excitation one. In our simulations, it has been set $E_{p_0} = 10^{-4}\Gamma\sqrt{2/\Gamma_{1D}}$. Again, as long as we are in the weak driving regime, the transmitted intensity and second-order correlation functions are independent of this specific choice.

4.5. Simulation of the experiment—triangular pulse

Analogously, to quantitatively reproduce the triangular pulse dynamics in figure 4, we add the motional dephasing γ_r of the Rydberg atoms to the spin model and consider finite blockade. We set D, D_b, Ω_c, and γ_r to the values given in section 3 and reproduce well the measured output intensity of the system, as shown in

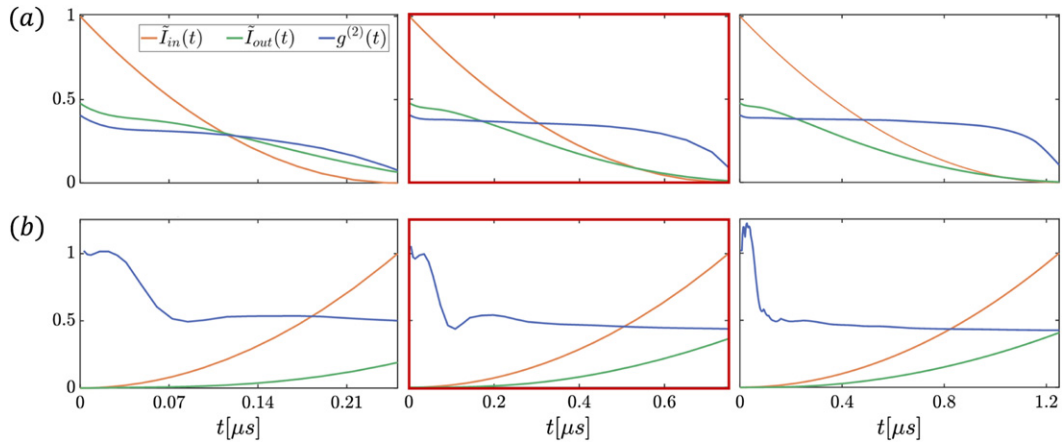

Figure 10. Numerical analysis of the photon statistics for triangular pulses of different slopes. (a) The system begins in the steady state and the input field is decreased linearly. (b) The system is in the ground state and the input field is increased linearly up to E_{p_0} (i.e. $\tilde{I}_{\rm in} = 1$). D, $D_{\rm b}$, $\gamma_{\rm r}$, and $\Omega_{\rm c}$ are set to the experimental values of section 3. The time-dependent input intensity, $\tilde{I}_{\rm in}(t)$, output intensity $\tilde{I}_{\rm out}(t)$, and second-order correlation function $g^{(2)}(t)$ are denoted by the solid orange, green, and blue curves, respectively. The middle panels exhibit almost the same slopes of the triangular pulse as the experimental pulses in figure 4.

the insets of figure 4. Our numerically simulated second-order correlation functions $g^{(2)}(t)$ also qualitatively agree with the detected $g^{(2)}_{\Delta t}(t)$. The peak amplitude value E_{p_0} has been set to $10^{-4}\Gamma\sqrt{2/\Gamma_{\rm 1D}}$ in the simulations.

To better understand the dynamics for the triangular pulse with negative slope, numerically we can consider a related situation, where a pulse of constant amplitude is sent in until the system reaches steady state, before the input pulse is then gradually shut off in a triangular fashion. In figure 10(a) we show the simulated output field properties, varying the slope in the three panels from a fast decrease to slow. Here, we have set the system parameters $D, D_{\rm b}, \gamma_{\rm r}$, and $\Omega_{\rm c}$ to the experimental values listed in section 3, while the slope in the middle panel closely corresponds to that in figure 4(a). For the fast decreasing slope, the atomic medium cannot equilibrate with the decreasing pulse amplitude, and thus a gradual decrease of $g^{(2)}(t)$ is clearly visible, similar to the transient behavior following the turn off of a square pulse presented in section 4.3. For the slowest decaying slope, $g^{(2)}(t)$ is essentially constant in time and identical to the steady state value. It can be seen that the negative slope closely matching the experimental situation (middle panel of figure 10(a)) corresponds to an intermediate situation, which exhibits both a temporal region where $g^{(2)}(t)$ remains close to its ss value, while exhibiting a transient decrease later.

We then perform a similar analysis, simulating an atomic system that begins in its ground state and a triangular input field of different slopes is turned on. The results are plotted in figure 10(b), again varying the slope from fast to slow. In all cases considered, the second-order correlation function $g^{(2)}(t)$ exhibits a transient behavior right at the turn on, before settling to its ss value even as the pulse continues to increase. We observe that the initial transient occurs during a comparable time scale as the instantaneous turn-on case analyzed in figure 7.

5. Single-photon generation and storage

The turn-off transient, where $g^{(2)}_{\Delta t}(t)$ strongly decreases, opens the way for possible applications related to narrowband single-photon generation. For that purpose, we could cut the output pulses and exploit the single photons arriving in the last part of the pulse. To analyze this proposal, we select a temporal window at the end of the pulse when looking for detection counts and coincidences. Then, we measure the $g^{(2)}_{\Delta t}(t)$ values of the photons arriving inside this window and their corresponding detection and generation probability. The generation probability is inferred as $P_{\rm g} = N_1/\eta_{\rm det}$, where N_1 is the number of counts per trial arriving to $\rm SPD_1$ in the selected time window and $\eta_{\rm det}$ is the detection efficiency, including fiber coupling, transmission through all the optical elements and single-photon detector efficiency. Figure 11 shows an example of the single-photon generation for a time window $\Delta t = 500$ ns and $t = 1.2$ μs (see inset plot). When measuring the normalized coincidences for consecutive pulses (see figure 11(a)), we get a value of $g^{(2)}_{\Delta t} = 0.218 \pm 0.015$ significantly lower than for $\Delta t = 1.6$ μs. Moreover, the time resolved measurement within one pulse (see figure 11(b)) shows that the values of $g^{(2)}(\tau)$ remain low for the full window, showing the generation of a localized single photon.

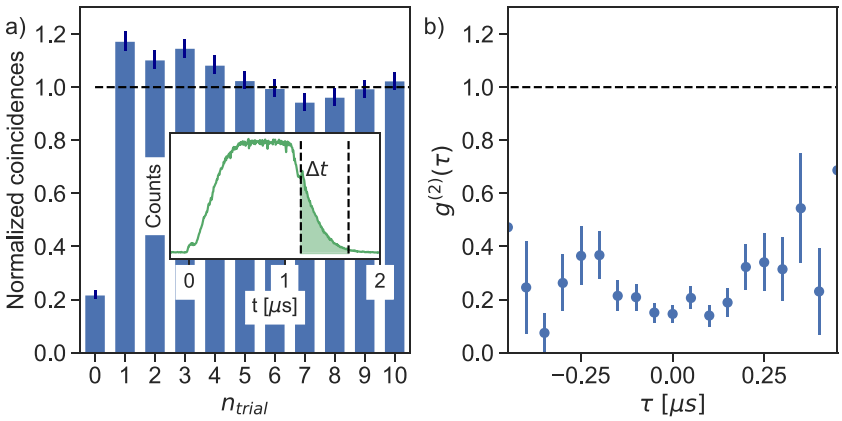

Figure 11. Single-photon generation: example of single-photon generation with $\Delta t = 500$ ns. (a) Normalized coincidence counts between different trials, leading to a value of $g^{(2)}_{\Delta t} = 0.218 \pm 0.015$ for $n_{\text{trial}} = 0$. (b) Time-resolved measurement of $g^{(2)}(\tau)$ leading to a zero-delay value of $g^{(2)}(0) = 0.15 \pm 0.03$. Error bars correspond to one standard deviation.

To further study the effect of the temporal window, we then vary Δt, while keeping the final time $t + \Delta t = 1.7$ μs fixed. Figure 12 shows the results for different duration of the temporal window, for Gaussian and square input pulses. When we increase the time window, the probability to have a detection count increases, but at the expense of reducing the quality of the single photons. For the previously studied square pulse, $g^{(2)}_{\Delta t}(t) = 0.48 \pm 0.01$ is obtained for $\Delta t = 0.68$ μs and a generation probability of 0.145 ± 0.014, while $g^{(2)}_{\Delta t}(t) = 0.147 \pm 0.017$ is obtained for $\Delta t = 0.45$ μs and a generation probability of 0.046 ± 0.004. We compare the results for the square pulse with the case of a Gaussian input pulse. We see that the Gaussian pulse leads to a higher value of $g^{(2)}_{\Delta t}(t)$, for all generation efficiencies, compared to the square pulse. This confirms that a fast shutoff of the input pulse is beneficial for the production of single photons.

We also compare the results with the strategy consisting of storing the input Gaussian pulse in the Rydberg state [19, 41–43]. This can be made by switching off the control beam ($\Omega_c \to 0$) when polaritons are traveling inside the medium. After a storage time of $t_S = 500$ ns, we can retrieve the output pulse by switching on again the control beam. This method allows for an increase in the quantum character of the output pulse without changing the experimental conditions. Due to our limited D, the entire input pulse cannot be compressed inside the medium and only a part of the pulse can be stored as Rydberg excitations, importantly reducing the output efficiency. In figure 12, we show the $g^{(2)}_{\Delta t}$ obtained after storage and retrieval (in green), for Δt taking into account the whole retrieved pulse (see figure 12(a)). As we can observe, the $g^{(2)}_{\Delta t}$ in the storage case is similar to that obtained in the turn-off transient of the transmitted square pulse, for the same generation probability (see green and orange points of figure 12(b)). However, for lower quality of the output photons, i.e. higher values of $g^{(2)}_{\Delta t}$, the generation probability in the transient case importantly increases.

Finally, in figure 12(c) we plot $g^{(2)}_{\Delta t}$ as function of the inverse of Δt, which is proportional to the photon bandwidth. Values of $g^{(2)}(\Delta t) < 0.2$ can be achieved for $1/\Delta t \sim 2$ MHz, showing that high quality, narrowband single photons can be generated with this technique.

As shown in section 4, increasing the optical depth and reducing the Rabi frequency of the control field results in a better separation between the two-photon dynamics and the single-photon one and therefore leads to a smaller value of $g^{(2)}_{\Delta t}$ in the turn-off transient. However, the single-photon generation efficiency is currently affected by the low value of the transmission in the EIT transparency window, which is likely limited by the decoherence rate of the $|g\rangle$ to $|r\rangle$ transition, which also enforces a lower bound in the choice of Ω_c. We expect that reducing the laser linewidths by active stabilization on an optical cavity would yield a significant increase in the EIT transmission and also make lower choices of the Rabi frequency of the control laser possible. Moreover, a larger value of D_b would allow a more efficient compression of the pulse within a blockade radius. The current values of generation efficiency achieved (around 10%) are comparable with the values reported in single-photon generation experiments using off-resonant (Raman) excitation to the Rydberg states with cold atomic ensembles [18]. It is informative to compare this efficiency with probabilistic techniques of single-photon generation with atomic ensembles, such as e.g. the Duan–Lukin–Cirac–Zoller scheme [22]. This scheme generates probabilistically photon pairs in a two-mode squeezed state with a probability per trial p, where one of the photons is stored as a collective atomic spin excitation in the ensemble. Upon detection of the first photon which provides a heralding

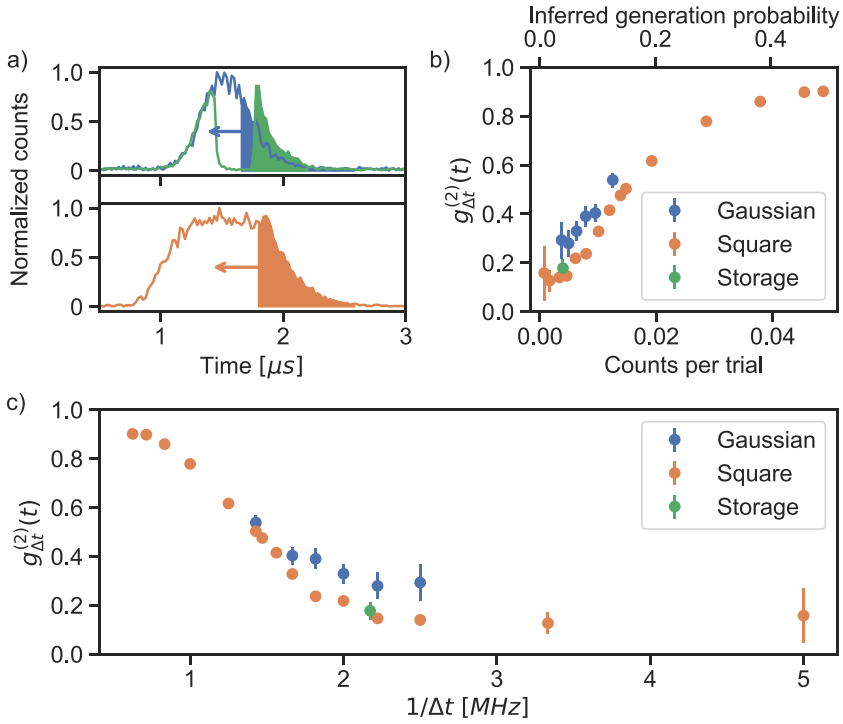

Figure 12. Single-photon generation. (a) Temporal distribution of a Gaussian pulse after propagation through EIT (in blue) and after storage (in green) and that of a square pulse after propagation through EIT (in orange). The temporal window is varied in plots (b) and (c) for the slow light case, as indicated by the arrow. (b) $g^{(2)}_{\Delta t}(t)$ as a function of the number of counts per trial in SPD_1 (bottom axis) and the probability to have a photon at the output of the cloud (upper axis), for an input Gaussian pulse (in blue), the previously shown square pulse (in orange) and after storing for 500 ns (in green). The generation probability is increased by taking the same final time of the temporal window but changing the starting time to increase Δt, as we can see in plot (a). (c) $g^{(2)}_{\Delta t}(t)$ as a function of the inverse of the temporal window, for the same cases as before. Vertical error bars correspond to one standard deviation.

signal, this collective spin excitation can then be efficiently transferred into a single photon in a well-defined spatio–temporal mode with an efficiency η_R. The probability to generate a single photon per trial is therefore given by $P_{DLCZ} = p\eta_D\eta_R$ where η_D is the probability to detect the first photon. For a perfect two-mode squeezed state and for $p \ll 1$, the second-order autocorrelation of the retrieved photon is $g^{(2)}(0) = 4p$. In the best-case scenario (i.e. with unity detection and read-out efficiency), a DLCZ source could generate a photon with $g^{(2)}(0) = 0.1$ with a probability of $P_{DLCZ} = 0.025$ per trial. In practice, with finite detection and read-out efficiencies, this value will be even lower. Therefore, even though the single-photon generation efficiency demonstrated in this paper is quite modest and could still be largely improved, it compare favorably to probabilistic schemes.

6. Conclusions

In this paper, we investigated the propagation of weak coherent pulses in a cold atomic ensemble in the regime of Rydberg EIT. We found experimentally that the second-order correlation function of the output pulse depends on the time throughout the pulse and varies during the transients of the pulse. In particular, the value of $g^{(2)}_{\Delta t}$ strongly decreases towards the end of the traveling pulse. Through a theoretical analysis, we were able to quantitatively predict the measured pulse dynamics, both at the linear and nonlinear level, and to provide a simple explanation, in the case of a perfectly square pulse propagating in a fully blockaded medium. Taking advantage of this behavior, we explored the possibility to generate localized single photons and showed that it has better efficiency than a probabilistic DLCZ-like source.

Acknowledgments

This project received funding from the Government of Spain via the MICINN plan nacional grants PID2019-106850RB-I00 and PGC2018-096844-B-I00, Severo Ochoa CEX2019-000910-S and AEI Europa Excelencia program (EUR2020-112155, project ENHANCE); from Fundació Cellex, Fundació Mir-Puig Generalitat de Catalunya (CERCA, AGAUR, project QuantumCat, ref. 001-P-001644), Gordon and Betty

Moore Foundation through Grant No. GBMF7446 to HdR and from European Union's Horizon 2020 research and innovation program under Grant Agreement No. 899275 (DAALI) Quantum Flagship project 820445 (QIA).

Data availability statement

The data that support the findings of this study are available upon reasonable request from the authors.

ORCID iDs

Auxiliadora Padrón-Brito https://orcid.org/0000-0003-0349-810X
Emanuele Distante https://orcid.org/0000-0001-5728-759X

References

[1] Saffman M, Walker T G and Mølmer K 2010 *Rev. Mod. Phys.* **82** 2313–63
[2] Wilk T, Gaetan A, Evellin C, Wolters J, Miroshnychenko Y, Grangier P and Browaeys A 2010 *Phys. Rev. Lett.* **104** 010502
[3] Levine H *et al* 2018 *Phys. Rev. Lett.* **121** 123603
[4] Isenhower L, Urban E, Zhang X L, Gill A T, Henage T, Johnson T A, Walker T G and Saffman M 2010 *Phys. Rev. Lett.* **104** 010503
[5] Maller K M, Lichtman M T, Xia T, Sun Y, Piotrowicz M J, Carr A W, Isenhower L and Saffman M 2015 *Phys. Rev.* A **92** 022336
[6] Bernien H *et al* 2017 *Nature* **551** 579–84
[7] Barredo D, Lienhard V, de Léséleuc S, Lahaye T and Browaeys A 2018 *Nature* **561** 79–82
[8] Peyronel T, Firstenberg O, Liang Q-Y, Hofferberth S, Gorshkov A V, Pohl T, Lukin M D and Vuletić V 2012 *Nature* **488** 57–60
[9] Firstenberg O, Peyronel T, Liang Q-Y, Gorshkov A V, Lukin M D and Vuletić V 2013 *Nature* **502** 71–5
[10] Paris-Mandoki A, Braun C, Kumlin J, Tresp C, Mirgorodskiy I, Christaller F, Büchler H P and Hofferberth S 2017 *Phys. Rev.* X **7** 041010
[11] Chang D E, Vuletić V and Lukin M D 2014 *Nat. Photon.* **8** 685–94
[12] Firstenberg O, Adams C S and Hofferberth S 2016 *J. Phys. B: At. Mol. Opt. Phys.* **49** 152003
[13] Tiarks D, Baur S, Schneider K, Dürr S and Rempe G 2014 *Phys. Rev. Lett.* **113** 1–5
[14] Gorniaczyk H, Tresp C, Schmidt J, Fedder H and Hofferberth S 2014 *Phys. Rev. Lett.* **113** 1–5
[15] Baur S, Tiarks D, Rempe G and Dürr S 2014 *Phys. Rev. Lett.* **112** 1–5
[16] Busche H, Huillery P, Ball S W, Ilieva T, Jones M P A and Adams C S 2017 *Nat. Phys.* **13** 655–8
[17] Tiarks D, Schmidt-Eberle S, Stolz T, Rempe G and Dürr S 2019 *Nat. Phys.* **15** 124–6
[18] Dudin Y O and Kuzmich A 2012 *Science* **336** 887–9
[19] Maxwell D, Szwer D J, Paredes-Barato D, Busche H, Pritchard J D, Gauguet A, Weatherill K J, Jones M P and Adams C S 2013 *Phys. Rev. Lett.* **110** 1–7
[20] Li A, Chang X, Huang Z, Li C, Wei Y, Zhang L, Wang T and Gong J 2016 *Angew. Chem., Int. Ed.* **55** 13618
[21] Li J, Zhou M T, Jing B, Wang X J, Yang S J, Jiang X, Molmer K, Bao X H and Pan J W 2016 *Phys. Rev. Lett.* **117** 180501
[22] Duan L-M, Lukin M D, Cirac J I and Zoller P 2001 *Nature* **414** 413–8
[23] Mohapatra A K, Jackson T R and Adams C S 2007 *Phys. Rev. Lett.* **98** 113003
[24] Petrosyan D, Otterbach J and Fleischhauer M 2011 *Phys. Rev. Lett.* **107** 213601
[25] Gorshkov A V, Nath R and Pohl T 2013 *Phys. Rev. Lett.* **110** 153601
[26] Moos M, Höning M, Unanyan R and Fleischhauer M 2015 *Phys. Rev.* A **92** 053846
[27] Zeuthen E, Gullans M J, Maghrebi M F and Gorshkov A V 2017 *Phys. Rev. Lett.* **119** 043602
[28] Sangouard N and Zbinden H 2012 *J. Mod. Opt.* **59** 1458–64
[29] Sangouard N, Simon C, Minář J C V, Zbinden H, de Riedmatten H and Gisin N 2007 *Phys. Rev.* A **76** 050301
[30] Knill E, Laflamme R and Milburn G J 2001 *Nature* **409** 46–52
[31] Craddock A N, Hannegan J, Ornelas-Huerta D P, Siverns J D, Hachtel A J, Goldschmidt E A, Porto J V, Quraishi Q and Rolston S L 2019 *Phys. Rev. Lett.* **123** 213601
[32] Maxwell D, Szwer D J, Paredes-Barato D, Busche H, Pritchard J D, Gauguet A, Jones M P A and Adams C S 2014 *Phys. Rev.* A **89** 043827
[33] Moehl C, Spong N L R, Jiao Y, So C, Ilieva T, Weidemueller M and Adams C S 2020 *J. Phys. B: At. Mol. Opt. Phys.* **53** 084005
[34] Steck D A 2001 *Rubidium 87 D Line Data*
[35] Bienias P *et al* 2020 *Phys. Rev. Res.* **2** 033049
[36] Ornelas-Huerta D P, Craddock A N, Goldschmidt E A, Hachtel A J, Wang Y, Bienias P, Gorshkov A V, Rolston S L and Porto J V 2020 *Optica* **7** 813–9
[37] Caneva T, Manzoni M T, Shi T, Douglas J S, Cirac J I and Chang D E 2015 *New J. Phys.* **17** 113001
[38] Manzoni M T, Chang D E and Douglas J S 2017 *Nat. Commun.* **8** 1743
[39] Bromley S L *et al* 2016 *Nat. Commun.* **7** 11039
[40] Svidzinsky A A, Chang J T and Scully M O 2010 *Phys. Rev.* A **81** 053821
[41] Distante E, Padrón-Brito A, Cristiani M, Paredes-Barato D and de Riedmatten H 2016 *Phys. Rev. Lett.* **117** 113001
[42] Distante E, Farrera P, Padrón-Brito A, Paredes-Barato D, Heinze G and de Riedmatten H 2017 *Nat. Commun.* **8** 14072
[43] Schmidt-Eberle S, Stolz T, Rempe G and Duerr S 2020 *Phys. Rev.* A **101** 013421